

Optimization Design of Interior Permanent Magnet Synchronous Motor with U-Shaped Rotor for Low-Level Torque Ripple and Electromagnetic Vibration

Zezhi Xing, Xiuhe Wang, Wenliang Zhao, *Member, IEEE*, Xian Li, Lixin Xiong, Xin Zhang

Abstract—The optimization design of the interior permanent magnet synchronous motor (IPMSM) is a challenge due to its complex rotor configuration and interdependent structural parameters. The electromagnetic vibration of the IPMSM is intricate due to the complex contents of electromagnetic force densities caused by the unequal inductances between the d - and q -axes. In this paper, a 6-pole 36-slot IPMSM with a non-uniform air gap is designed, and the multi-objective stratified optimization method is used to optimize the stator and rotor structure parameters for the low-level torque ripple and electromagnetic vibration, which greatly improves the optimization efficiency. In addition, an improved iterative Taguchi method is proposed, the optimization ranges of variables are reasonably narrowed, the optimal structural parameters are found efficiently and accurately, and the superiority of the proposed method is verified by comparing with the optimization results obtained by the conventional Taguchi method. In addition, the complete analysis of the optimal motor, including losses, temperature distributions, and irreversible demagnetization of the permanent magnets (PMs), is performed, and the rationality of the optimization scheme is comprehensively verified. Finally, sufficient prototype tests are performed, and the prototype test results well verify the feasibility and effectiveness of the proposed optimization method and optimized motor structure.

Index Terms—Electromagnetic vibration, interior permanent magnet synchronous motor (IPMSM), iterative Taguchi method, multi-objective optimization.

I. INTRODUCTION

SINCE the interior rotor structure can make full use of the reluctance torque generated by the asymmetry of the rotor magnetic circuit and effectively improve the power density and dynamic performance of the motor, the interior permanent magnet synchronous motors (IPMSMs) have been widely used in high-performance electric drive applications [1]-[2].

This work was supported by the National Key Research and Development Program of China under grant 2022YFB2402800, the National Natural Science Foundation of China under grant 52077122, and the Taishan Industrial Experts Program. (Corresponding author: Xiuhe Wang).

Zezhi Xing, Xiuhe Wang, Wenliang Zhao, and Xian Li are with School of Electrical Engineering, Shandong University, Jinan, China. Lixin Xiong and Xin Zhang are with Shandong Kehui Power Automation Company Limited, Zibo, China (e-mail: wangxh@sdu.edu.cn).

However, the high air-gap flux density will inevitably lead to a torque ripple while generating large output torque, which will directly affect the stability of the motor [3]. The torque ripple of the IPMSMs can be well reduced by changing the rotor structure, such as adopting an asymmetric barrier [4], changing the magnetic pole width [5], shifting the magnetic pole [6], and adopting a segmented rotor [7], but they will lead to a complicated rotor structure and poor reliability. Therefore, it is particularly critical to fundamentally optimize the rotor geometry parameters.

In recent years, multiple intelligent optimization algorithms have been applied to the optimization design of IPMSMs. In [8]-[9], the NSGA-II algorithm is used to optimize the output torque and torque ripple. In [10], the motor structure parameters are divided into multiple optimization levels based on the sensitivity analysis, which are optimized separately. The neural networks of hub permanent magnet synchronous motors [11]-[12], IPMSMs with V-shaped rotor [13], and line-start permanent magnet synchronous motors [14] are established, and based on these the comprehensive performances of the motors are analyzed and optimized. The relatively optimal structural parameters of the motor can also be obtained well by using the response surface method [15] and the differential evolution algorithm [16]. Compared with intelligent optimization algorithms, the combination of the finite element method (FEM) and the Taguchi method has obvious advantages in the optimization design of the motor. It not only saves the complex programming process in the early stage, but also accurately considers the complex physical parameters of the motor and the influence of saturation. The V-shaped IPMSM [17], transverse flux machine [18], and claw pole alternator [19] are optimized by the Taguchi method. However, the initial variable ranges are determined artificially and widely, resulting in the optimization results not being optimal. Even though the optimization accuracy can be improved by increasing the number of levels of each variable, it is inefficient and time-consuming. In comparison, the range and the level of each variable should be reasonably reduced and updated according to the current optimal results to obtain the global optimal solutions. In order to overcome this, an improved iterative Taguchi method is proposed in this paper.

In addition, the electromagnetic vibration, which is one of the essential indicators for evaluating the reliability of the motor, is almost ignored due to the complex analysis processes including multiphysics such as electromagnetic and modal

analysis [20]-[21]. In IPMSM, the difference in d - & q -inductances complicates the harmonic contents of the air-gap magnetic field, which will lead to the complexity of the electromagnetic forces and then excite strong electromagnetic vibrations [22]-[24]. Therefore, the electromagnetic vibration of the motor must be evaluated during the optimal design stage.

This paper designs a 6-pole 36-slot IPMSM with a U-shaped rotor in Section II. In Section III, the optimization variables and objectives of the IPMSM are determined, and the stator and rotor structural parameters are optimized separately based on the improved iterative Taguchi method. In Section IV, the feasibility and effectiveness of the proposed optimization method and optimized motor structure are verified by the prototype tests. This paper is summarized in Section V.

II. MOTOR STRUCTURE AND PARAMETER DETERMINATION

According to the needs of the project, a 6-pole 36-slot IPMSM is designed to compare the electromagnetic performance with the previously designed 6-pole 36-slot surface-mounted permanent magnet synchronous motor (SPMSM) in [20], as shown in Fig. 1.

Draw lessons from the stator parameters of 6-pole 36-slot SPMSM of the same series, the initial selections of stator slot parameters considering the slot full ratio, inserting coils process, and tooth flux density are determined. The four common interior permanent magnet rotor topologies with spoke-shaped rotor, tangential-shaped rotor, V-shaped rotor, and U-shaped rotor are typical and most commonly used [25]. The U-shaped rotor can accommodate more permanent magnets (PMs) to increase the power density of the motor compared to the other three interior rotor topologies with same diameters. The delta, double-V, and double-U patterns for interior PM rotors can further improve the power density of the motor [26]-[27], but the rotor structures become more complex and the mechanical strengths of the rotors become worse, which also poses a higher challenge to the prototype processing. Finally, the U-shaped rotor topology is selected by comprehensively considering the magnetic focusing effect and manufacturing complexity, and the rotor geometric parameters that meet the requirements of magnetic flux leakage and mechanical strength are summarized in Table I.

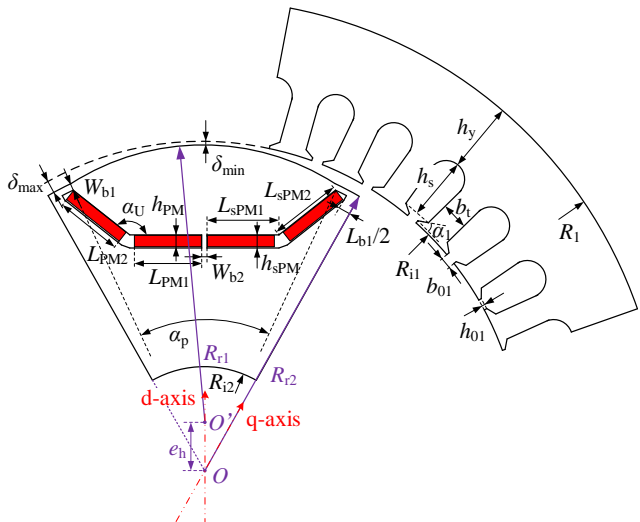


Fig. 1. Structural model of IPMSM.

TABLE I
MAIN PARAMETERS OF IPMSM

Par.	Description	Unit	Value
Rated	P_N	kW	11
	n_N	r/min	1500
	T_N	N m	70.03
	U_N	V	380
Stator	R_1/R_{r1}	Outer/inner radii	mm 130/90
	h_y	Yoke thickness	mm 18
	h_s	Slot depth	mm 19.7
	b_t	Tooth width	mm 7.7
	α_t	Slot shoulder angle	deg 30
	h_{01}	Slot opening height	mm 0.8
	b_{01}	Slot opening width	mm 3.2
Rotor	$\delta_{\max}/\delta_{\min}$	Max/min air gaps	mm 1/0.5
	R_{r2}	Inner radius	mm 30
	L_{sPM1}/L_{sPM2}	Lengths of PM slot	mm 20.4/20.4
	h_{sPM}	Height of PM slot	mm 3.8
	α_u	U-shaped angle	deg 138.45
	α_p	Polar arc angle	deg 48
	W_{b1}/W_{b2}	Widths of magnetic bridge	mm 1.5/1.5
	L_{b1}	Length of magnetic bridge	mm 9.82
	L_{PM1}/L_{PM2}	Lengths of PM	mm 19/19
	h_{PM}	Height of PM	mm 3.5

In order to effectively reduce the harmonic content of no-load air-gap flux density and improve the comprehensive performance of the motor, the rotor with a non-uniform air gap is designed. Within the pole arc range, the center O' of the outer arc of the rotor core does not coincide with the center O of the motor and shifts e_h along the d-axis direction, the radius of the outer arc is R_{r1} . The center of the outer arc of the rotor core outside the pole arc range is the motor center O and the radius is R_{r2} . Therefore, the IPMSM has a minimum air gap δ_{\min} in the d-axis direction and a maximum air gap δ_{\max} in the q-axis direction. r_δ is the non-uniform air gap ratio, where $r_\delta = \delta_{\max}/\delta_{\min}$.

III. ANALYSIS OF TORQUE RIPPLE AND ELECTROMAGNETIC VIBRATIONS

A. Torque ripple

The cogging torques T_{cog} , one of the main sources of torque ripple, are shown in Fig. 2(a). The air-gap flux densities of the IPMSM with a slotless stator are shown in Fig. 3(a). In this case, the air-gap flux density waveform $B(\alpha)$ is exactly the same as that of air-gap magnetomotive force (MMF) $F(\alpha)$, α represents circumferential direction. The harmonic amplitudes of $B^2(\alpha)$ with different non-uniform air gap ratio r_δ are obtained by Fourier decomposition of $B^2(\alpha)$, as shown in Fig. 3(b). For the 6-pole 36-slot IPMSM in this paper, the harmonic components F_m of $F^2(\alpha)$ that affect the cogging torques are F_6 , F_{12} , $F_{18} \dots$ [28]. It can be seen that when $r_\delta=2$, B_6 , B_{12} , $B_{18} \dots$ in the harmonic components of $B^2(\alpha)$ are reduced, that is, F_6 , F_{12} , $F_{18} \dots$ are also reduced, so the cogging torque is greatly reduced by adopting a non-uniform air gap.

The no-load back electromotive forces (EMFs) and their harmonic components are shown in Fig. 4. Due to the PMs being internal and their sizes being constant with different r_δ , the effective values of the fundamental waves of no-load back EMFs change slightly when $r_\delta=2$. The rated performance of the motor is closely related to the control strategy, and the motor performance on load analyzed in this paper is the properties

under the control mode of Maximum Torque Per Ampere (MTPA). For the 6-pole 36-slot IPMSM in this paper, the internal power factor angles corresponding to the minimum currents are 30.4° and 29.6° when r_δ is 1 and 2. The electromagnetic torques under the current source excitations with the same amplitudes (17.8A) and different internal power factor angles (30.4° and 29.6°) are shown in Fig. 2(b). It can be seen that the torque ripple is effectively reduced due to the low-order harmonics of the no-load EMF being effectively weakened when $r_\delta=2$, while the average torque is reduced from 70.86N m to 70.15N m, but the decrease is slight.

B. Electromagnetic vibrations

The electromagnetic vibrations are mainly excited by the electromagnetic force waves acting on the stator teeth. The research points out that increasing the switching frequency can effectively reduce the vibrations near the switching frequency caused by the high-frequency current harmonics for the motors powered by the inverter, and the maximum vibration accelerations of the motor are transferred to the vicinity of the natural frequencies of stator [20]. Therefore, the subsequent analysis ignores the impact of high-frequency harmonic currents and focuses on exploring the inherent electromagnetic vibrations of the IPMSM under the action of magnetic fields generated by PMs and low-frequency currents.

1) Analysis of electromagnetic forces

The MMFs $F_1(\alpha, t)$ and $F_2(\alpha, t)$ generated by the PMs and the low-frequency harmonic currents can be expressed as [29]

$$F_1(\alpha, t) = F_{1r}(\alpha, t) + jF_{1t}(\alpha, t) \\ = \sum_{\mu=1,3,5...} \left[F_{1r_\mu} \cos(\mu\omega t - \mu p\alpha) + jF_{1t_\mu} \sin(\mu\omega t - \mu p\alpha) \right] \quad (1)$$

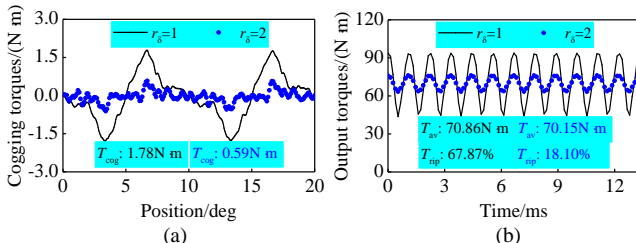


Fig. 2. (a) Cogging torques and (b) electromagnetic torques of IPMSM.

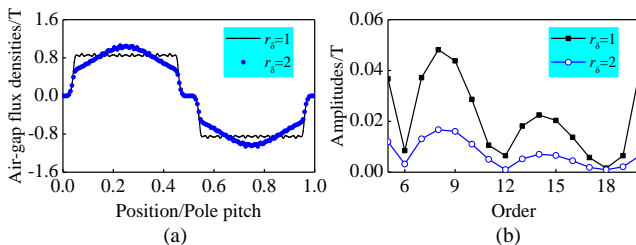


Fig. 3. (a) Air-gap flux densities $B(\alpha)$ of the IPMSM with the slotless stator and (b) the harmonic components of $B^2(\alpha)$.

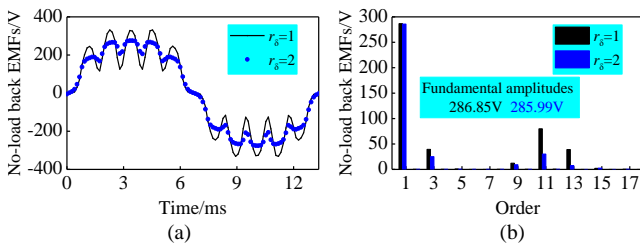


Fig. 4. (a) No-load back EMFs and (b) their harmonic components.

$$F_2(\alpha, t) = F_{2r}(\alpha, t) + jF_{2t}(\alpha, t) \\ = \sum_{l=1\pm 6h, h=0,1,2...} \left[F_{2r_v} \sin(l\omega t - vp\alpha + \phi_{2v}) \right. \\ \left. + jF_{2t_v} \cos(l\omega t - vp\alpha + \phi_{2v}) \right] \quad (2)$$

where j is an imaginary operator, ω and p are the electrical angular frequency and pole pairs number. F_{1r_μ} and F_{1t_μ} are the amplitudes of the μ -th harmonics of the radial components $F_{1r}(\alpha, t)$ and $F_{1t}(\alpha, t)$ of $F_1(\alpha, t)$, and F_{2r_v} and F_{2t_v} are the amplitudes of the v -th harmonics of $F_{2r}(\alpha, t)$ and $F_{2t}(\alpha, t)$, ϕ_{2v} is the phase angle.

The total air-gap permeance $\Lambda(\alpha, t)$ considering stator slotting, non-uniform air gap, and rotor slotting can be expressed as [29]

$$\begin{aligned} \Lambda(\alpha, t) &= \Lambda_0 \cdot \lambda_s(\alpha) \cdot \lambda_{r1}(\alpha, t) \cdot \lambda_{r2}(\alpha, t) \\ &= \Lambda_0 \cdot \left\{ \lambda_{sr_0} + \sum_{m=1,2,3...} \left[\lambda_{sr_m} \cos(mQ_1\alpha) + j\lambda_{sr_m} \sin(mQ_1\alpha) \right] \right\} \cdot \\ &\quad \left\{ \lambda_{r1r_0} + \sum_{n=1,2,3...} \left[\lambda_{r1r_n} \cos 2n(p\alpha + \omega t) + j\lambda_{r1r_n} \sin 2n(p\alpha + \omega t) \right] \right\} \cdot \\ &\quad \left\{ \lambda_{r2r_0} + \sum_{g=1,2,3...} \left[\lambda_{r2r_g} \cos 2g(p\alpha + \omega t) + j\lambda_{r2r_g} \sin 2g(p\alpha + \omega t) \right] \right\} \end{aligned} \quad (3)$$

where $\Lambda_0 = \mu_0 / \delta_{\min}$, λ_s , λ_{r1} , and λ_{r2} are the relative permeance coefficients introduced by stator slotting, non-uniform air gap, and rotor slotting. Q_1 is the number of slots. λ_{sr_0} , λ_{r1r_0} , and λ_{r2r_0} are the amplitudes of constant components of λ_s , λ_{r1} , and λ_{r2} . λ_{sr_m} , λ_{r1r_n} , λ_{r2r_g} and λ_{st_m} , λ_{r1t_n} , λ_{r2t_g} are the amplitudes of m , n , g -th radial and tangential harmonics of λ_s , λ_{r1} , and λ_{r2} .

According to the Maxwell stress tensor method, the electromagnetic force densities in the air gap of the motor can be calculated by

$$\begin{aligned} p(\alpha, t) &= \frac{B^2(\alpha, t)}{2\mu_0} = \frac{\{[F_1(\alpha, t) + F_2(\alpha, t)] \cdot \Lambda^*(\alpha, t)\}^2}{2\mu_0} \\ &= \underbrace{\frac{1}{2\mu_0} [F_1(\alpha, t) \cdot \Lambda^*(\alpha, t)]^2}_{\text{Category 1}} + \underbrace{\frac{1}{2\mu_0} [F_2(\alpha, t) \cdot \Lambda^*(\alpha, t)]^2}_{\text{Category 2}} \\ &\quad + \underbrace{\frac{1}{\mu_0} F_1(\alpha, t) \cdot F_2(\alpha, t) \cdot \Lambda^{*2}(\alpha, t)}_{\text{Category 3}} \end{aligned} \quad (4)$$

where $B(\alpha, t)$ is air-gap flux density, $\Lambda^*(\alpha, t)$ is the conjugate of permeance $\Lambda(\alpha, t)$, μ_0 is vacuum permeability.

The specific components contained in the three categories of electromagnetic force densities in (4) are listed in Table II. f_1 is the fundamental frequency corresponding to ω . The harmonic contents of radial and tangential electromagnetic force densities are exactly the same.

The main low-order components of the radial and tangential electromagnetic force densities with no load and rated load are presented in Fig. 5 and Fig. 6. The amplitudes of the main low-order components of the electromagnetic force densities are listed in Table III. Consistent with analysis results, the order and frequency components of the no-load electromagnetic force densities are $(2h_1p \pm h_2Q_1)$ and $2h_1f_1$ ($h_1, h_2=0, 1, 2, 3, \dots$), and the order components of $[(2h_1 \pm 6k)p \pm h_2Q_1]$ corresponding to $2h_1f_1$ will be added under the action of the armature MMF.

The amplitudes of the components of $0p-0f_1$ in the radial electromagnetic force densities are the largest. But in the tangential electromagnetic force densities, the amplitudes of the components mainly generated by the low-order harmonic components of the air-gap permeance are the largest. When the non-uniform air gap with $r_\delta=2$ is adopted, the amplitudes of the

TABLE II
SPECIFIC COMPONENTS OF ELECTROMAGNETIC FORCE DENSITIES

Source	Frequency	Order
Categ.1	$(\mu_1 \pm \mu_2)f_1$	$(\mu_1 \pm \mu_2)p$
		$(\mu_1 \pm \mu_2)p \pm mQ_1$
	$[\mu_1 \pm \mu_2 \pm 2(n_1 \pm n_2)]f_1$	$[\mu_1 \pm \mu_2 \pm 2(n_1 \pm n_2)]p$
		$[\mu_1 \pm \mu_2 \pm 2(n_1 \pm n_2)]p \pm mQ_1$
	$[\mu_1 \pm \mu_2 \pm 2(g_1 \pm g_2)]f_1$	$[\mu_1 \pm \mu_2 \pm 2(g_1 \pm g_2)]p$
		$[\mu_1 \pm \mu_2 \pm 2(g_1 \pm g_2)]p \pm mQ_1$
Categ.2	$[\mu_1 \pm \mu_2 \pm 2(n_1 \pm n_2) \pm 2(g_1 \pm g_2)]f_1$	$[\mu_1 \pm \mu_2 \pm 2(n_1 \pm n_2) \pm 2(g_1 \pm g_2)]p$
		$[\mu_1 \pm \mu_2 \pm 2(n_1 \pm n_2) \pm 2(g_1 \pm g_2)]p \pm mQ_1$
	$(l_1 \pm l_2)f_1$	$(v_1 \pm v_2)p$
		$(v_1 \pm v_2)p \pm mQ_1$
	$[l_1 \pm l_2 \pm 2(n_1 \pm n_2)]f_1$	$[v_1 \pm v_2 \pm 2(n_1 \pm n_2)]p$
		$[v_1 \pm v_2 \pm 2(n_1 \pm n_2)]p \pm mQ_1$
Categ.3	$[l_1 \pm l_2 \pm 2(g_1 \pm g_2)]f_1$	$[v_1 \pm v_2 \pm 2(g_1 \pm g_2)]p$
		$[v_1 \pm v_2 \pm 2(g_1 \pm g_2)]p \pm mQ_1$
	$(\mu \pm l)f_1$	$(\mu \pm v)p$
		$(\mu \pm v)p \pm mQ_1$
	$[\mu \pm l \pm 2(n_1 \pm n_2)]f_1$	$[\mu \pm v \pm 2(n_1 \pm n_2)]p$
		$[\mu \pm v \pm 2(n_1 \pm n_2)]p \pm mQ_1$
	$[\mu \pm l \pm 2(g_1 \pm g_2)]f_1$	$[\mu \pm v \pm 2(g_1 \pm g_2)]p$
		$[\mu \pm v \pm 2(g_1 \pm g_2)]p \pm mQ_1$
	$[\mu \pm l \pm 2(n_1 \pm n_2) \pm 2(g_1 \pm g_2)]f_1$	$[\mu \pm v \pm 2(n_1 \pm n_2) \pm 2(g_1 \pm g_2)]p$
		$[\mu \pm v \pm 2(n_1 \pm n_2) \pm 2(g_1 \pm g_2)]p \pm mQ_1$

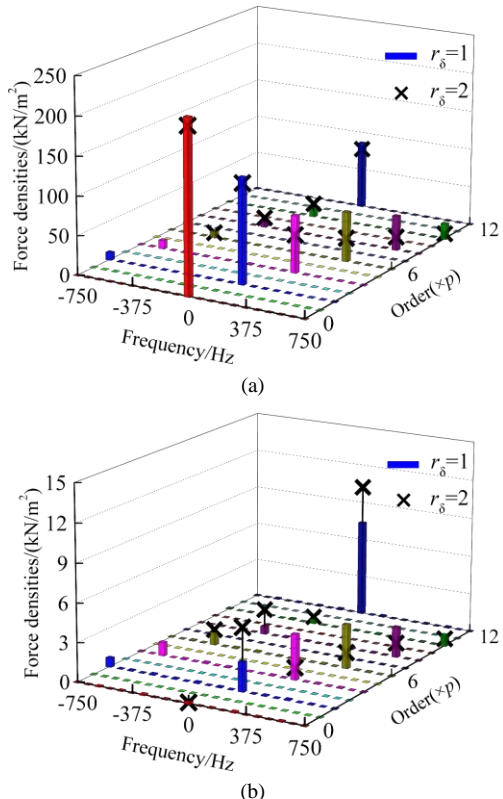


Fig. 5. Main low-order components of (a) radial and (b) tangential no-load electromagnetic force densities.

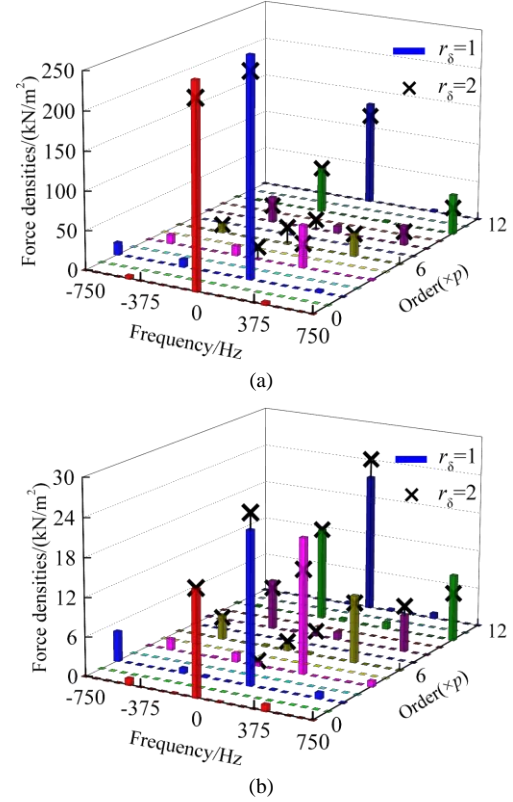


Fig. 6. Main low-order components of (a) radial and (b) tangential electromagnetic force densities with rated load.

TABLE III
AMPLITUDES OF MAIN COMPONENTS OF ELECTROMAGNETIC FORCE DENSITIES WITH NO LOAD AND RATED LOAD

Components	Radial/(kN/m²)		Tangential/(kN/m²)		
	$r_\delta=1$	$r_\delta=2$	$r_\delta=1$	$r_\delta=2$	
No load	(0p, 0f ₁)	221.80	210.34	0.21	0.07
	(2p, 2f ₁)	134.99	126.89	2.28	4.83
	(4p, 4f ₁)	73.20	47.84	3.51	0.88
	(6p, 6f ₁)	63.76	29.16	3.40	1.18
	(8p, 8f ₁)	44.51	16.28	2.35	1.05
	(10p, -2f ₁)	8.94	16.38	0.37	0.49
Rated load	(12p, 0f ₁)	86.09	77.27	7.38	10.21
	(0p, 0f ₁)	260.68	238.02	16.33	16.01
	(2p, 2f ₁)	279.38	258.63	23.45	25.91
	(4p, 4f ₁)	54.79	30.24	20.80	15.92
	(6p, 0f ₁)	2.05	21.42	1.07	1.34
	(6p, 6f ₁)	29.75	28.07	10.38	9.15
	(8p, 8f ₁)	25.29	16.61	5.69	6.98
	(10p, -2f ₁)	58.77	57.43	14.19	14.19
	(12p, 0f ₁)	131.83	115.29	21.24	24.06

tangential components of $2p-2f_1$ and $12p-0f_1$ are inevitably increased due to the amplitudes of the fundamental and the 11th-order harmonic components of the tangential air-gap flux density become larger, but the amplitudes of some low-order force density components are obviously reduced.

2) Analysis of stator natural frequencies

The equivalent material parameters of the laminated core and the windings wound with multiple coils show obvious anisotropy, which can be estimated according to the parameter calculation method of composite material. The equivalent elastic modulus E_z of the laminated core can be obtained by the Reuss series principle and E_r and E_a can be obtained by the Voigt parallel principle, namely [21]

TABLE IV

MODELS AND ORTHOTROPIC MATERIAL PARAMETERS OF STATOR

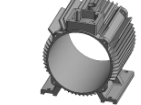
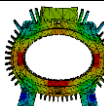
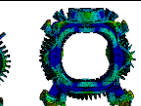
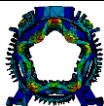
	Stator core	Windings	Enclosure
Finite element models			
Parameters	$E_r, E_\theta/\text{GPa}$	194.90	1.92
	E_z/GPa	46.95	77.75
	G_{rz}/GPa	76.73	0.94
	$G_{rz}, G_{\theta z}/\text{GPa}$	18.15	29.91
	$\mu_{r\theta}$	0.27	0.30
	μ_r, μ_z	0.07	0.007
	$\rho/(\text{kg}/\text{m}^3)$	7522.50	4766.83
			6821

TABLE V

NATURAL FREQUENCIES OF ENTIRE STATOR

Order	2nd	3rd	4th
Modal shapes			
Natural frequencies/Hz	674.37	1631.10	3109.30
Order	5th	0	6th
Modal shapes			
Natural frequencies/Hz	4780.70	5675.90	6699.20

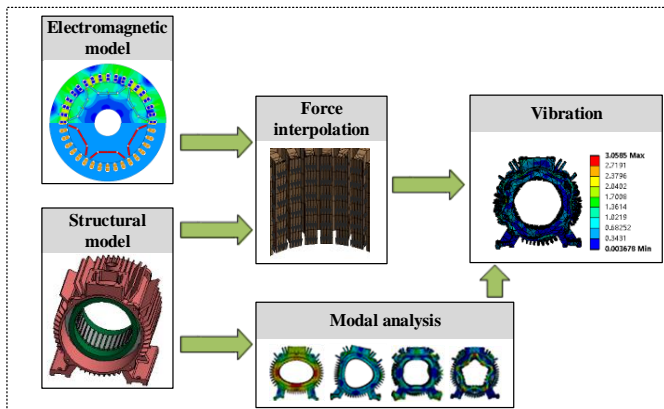


Fig. 7. Calculation flowchart of electromagnetic vibration.

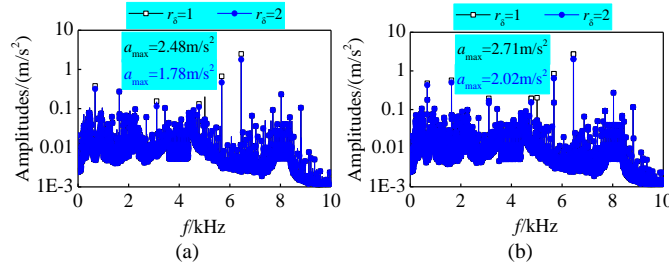


Fig. 8. Vibration accelerations of the IPMSM with (a) no load and (b) rated load.

$$E_z = \left(\frac{\xi_1}{E_1} + \frac{\xi_2}{E_2} \right)^{-1} \quad (5)$$

$$E_r = E_a = \xi_1 E_1 + \xi_2 E_2 \quad (6)$$

where ξ_1 and ξ_2 are the proportions of two materials, E_1 and E_2 are the elastic moduli of two materials, r and z represent radial and axial directions, respectively.

Similarly, the equivalent shear modulus G and Poisson's ratio μ of the laminated core can be obtained by

$$\mu_{ra} = \xi_1 \mu_1 + \xi_2 \mu_2 \quad (7)$$

$$G_{ra} = \frac{E_r}{2(1+\mu_{ra})} \quad (8)$$

$$G_{rz} = G_{az} = \left[\frac{2\xi_1(1+\mu_1)}{E_1} + \frac{2\xi_2(1+\mu_2)}{E_2} \right]^{-1} \quad (9)$$

where μ_1 and μ_2 are the Poisson's ratios of two materials.

The finite element models and the equivalent elastic modulus E , shear modulus G , and Poisson's ratio μ of the stator are shown in Table IV. The natural frequencies of the entire stator including the stator core, windings, and enclosure are calculated by the FEM, as shown in Table V.

3) Analysis of electromagnetic vibrations

Starting from the mechanism of noise generation, namely motor vibration, reducing the electromagnetic vibration of the motor can effectively improve the vibration and noise of the motor. Considering the verification of the optimization effect of motor vibration and noise based on prototype testing, the vibration accelerations before and after the optimization of the motor can be easily measured by the acceleration sensors attached to the surface of the enclosure, and the test results can directly reflect the optimization effect of the motor, which is more reliable than directly testing the sound pressure levels due to the test results are not affected by external interference. Therefore, the electromagnetic vibrations of the 6-pole 36-slot IPMSM are analyzed and optimized rather than the sound pressure levels.

The calculation flowchart of electromagnetic vibration is shown in Fig. 7. By applying the obtained electromagnetic forces to the corresponding stator teeth, the vibration accelerations of the stator can be obtained. The acceleration spectrums of the outer surface of the stator are shown in Fig. 8. The maximum vibration accelerations occur near the 6th-order natural frequency of the stator, and they are slightly larger with the rated load. Furthermore, the maximum vibration accelerations of the motor can be reduced by designing the non-uniform air gap. The main frequency components in the 6th-order electromagnetic force are $(2 \pm 12m)f_1$, thus the maximum vibration acceleration is mainly excited by the electromagnetic force density component of $2p-86f_1$. Therefore, weakening the component of $2p-86f_1$ of the electromagnetic force is one of the measures to effectively reduce electromagnetic vibration.

IV. MULTI-OBJECTIVE STRATIFIED OPTIMIZATION

A. Optimization objectives

In order to improve the working stability of the motor, the torque ripple T_{rip} and cogging torque T_{cog} are undoubtedly selected as the primary optimization objectives. Furthermore, it is inevitable to reduce the average electromagnetic torque T_{av} of the motor when optimizing the cogging torque and the torque ripple. Therefore, the average electromagnetic torque must be tracked during optimization.

According to the mechanism of electromagnetic vibration, the component of $2p-86f_1$ of the electromagnetic force densities

needs to be reduced, and the 6th-order natural frequency f_{n_6} of the stator should be adjusted so that it is far away from the frequencies of the electromagnetic force densities, scilicet making f_{n_6} away from $86f_1$ and $94f_1$ in this paper. The natural frequency of the stator is only related to the stator parameters, and the amplitude of the dominant component of electromagnetic force densities generated by the air-gap flux densities is more sensitive to the harmonic MMFs generated by the PMs. Therefore, in the stratified optimization process of stator and rotor parameters, considering the natural frequency of the stator and the amplitude of the dominant component of electromagnetic force densities separately can improve the optimization efficiency and maximize the improvement of electromagnetic vibration of the motor, the advantages of stratified optimization can be further expanded, which is also one of the significances of stratified optimization in this paper. Finally, the objective functions of the stator and rotor structure parameters optimization are determined as

$$\min_1: T_{\text{rip}}, 1/T_{\text{av}}, T_{\text{cog}}, |f_{n_6} - 90f_1| \quad (10)$$

$$\min_2: T_{\text{rip}}, 1/T_{\text{av}}, T_{\text{cog}}, P_{2p-86f_1} \quad (11)$$

B. Optimization variables

The inner and outer diameters of the stator core are crucial design parameters. However, the natural frequencies of the stator are very sensitive to the inner and outer diameters of the stator core. Adjusting the inner and outer diameters of the stator core can greatly change the natural frequencies of the stator, which will change the frequency band in which the maximum electromagnetic vibration acceleration occurs and the electromagnetic force wave component that plays a major role in electromagnetic vibration, making the weakening of electromagnetic vibration more difficult and complex. In addition, the adjustment of the inner diameter of the stator core means that there will be significant changes in the air gap length or the size of the PMs, which has a significant impact on the electromagnetic performance of the motor. The optimization process is similar to the redesign of another 6-pole 36-slot IPMSM, and the comparability with the motor using the initial scheme is reduced. In comprehensive consideration, this paper does not change the inner and outer diameters of the stator core during the optimal design of the motor. The variance-based sensitivity analysis of each optimization objective to the remaining structural parameters of the stator is shown in Fig. 9. When analyzing the sensitivity of each optimization objective to variable h_y , h_s changes synchronously with h_y , any one can be selected as an optimization variable. The minor change in α_1 also causes a change in h_s , while h_y remains unchanged. It can be seen that α_1 is not sensitive enough to each optimization objective, thus the main optimization variables of the stator are h_y , b_t , h_{01} , and b_{01} .

Familiarly, the rotor flux leakage can be effectively reduced by narrowing W_{b1} and W_{b2} . However, W_{b1} and W_{b2} are limited to more than 1mm to ensure sufficient mechanical strength. In order to simplify the manufacturing process of the PMs and reduce the optimization variables reasonably, make $L_{\text{PM1}} = L_{\text{PM2}}$ and $L_{\text{sPM1}} = L_{\text{sPM2}}$. For any given α_p , h_{SPM} , and L_{SPM} , α_u and L_{b1} are also uniquely determined. Therefore, the optimization variables for the rotor are W_{b1} , W_{b2} , α_p , L_{SPM} , h_{SPM} , and r_δ .

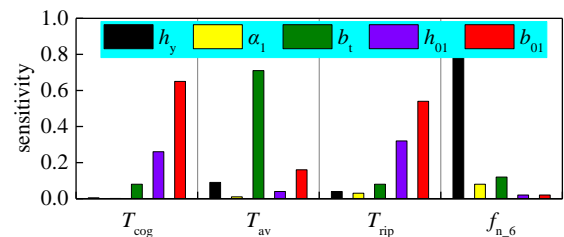


Fig. 9. Variance-based sensitivity analysis.

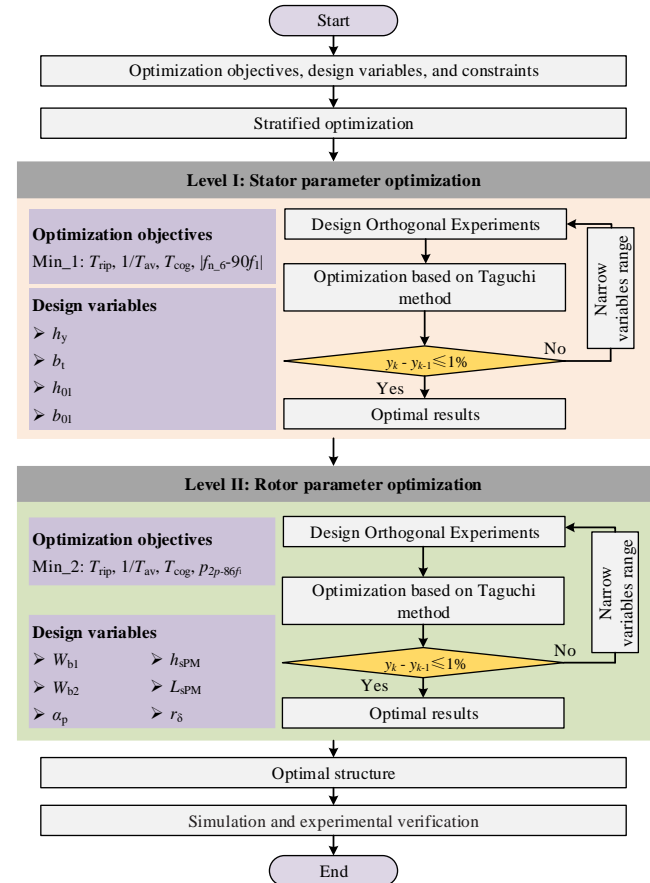


Fig. 10. Flowchart of multi-objective stratified optimization.

C. Multi-objective stratified optimization

Evaluating comprehensively the optimization effect and efficiency of the motor, the overall optimization process is divided into two levels, the stator and rotor structural parameters are optimized respectively based on the improved iterative Taguchi method, as shown in Fig. 10. It should be noted that, it is necessary to first optimize the stator parameters and accurately determine the stator natural frequencies, and then optimize the rotor parameters based on the determined stator natural frequencies to reduce the electromagnetic force density component that plays a major role in electromagnetic vibration.

1) Stator parameter optimization

The design of orthogonal experiments can solve commendably the problems of the consuming and inefficient analysis caused by the numerous variable combinations in multi-variable optimization. The specific values of h_y , b_t , h_{01} , and b_{01} are shown in Table VI. According to the orthogonal table L_{16} (4^4), 16 variable combinations are determined, and the

corresponding performances are analyzed by the FEM, as shown in Table VII.

The average value of an optimization objective under each level of each optimization variable can be calculated by

$$y_{ov_av} = \frac{1}{4} \sum_{i=1}^4 y_{ov}(i) \quad (12)$$

TABLE VI
LEVELS OF FOUR VARIABLES

Variables	Level 1	Level 2	Level 3	Level 4
h_y	16	18	20	22
b_t	7	8	9	10
h_{01}	0.6	0.8	1	1.2
b_{01}	2.5	3	3.5	4

TABLE VII
16 VARIABLE COMBINATIONS AND CORRESPONDING PERFORMANCES

Set	Variables				Performances			
	h_y (mm)	b_t (mm)	h_{01} (mm)	b_{01} (mm)	T_{cog} (N m)	T_{av} (N m)	T_{rip} (%)	$ f_{n_6-6750} $ (Hz)
1	16	7	0.6	2.5	1.08	68.56	35.23	6671.6
2	16	8	0.8	3	1.27	69.25	38.38	6668.3
3	16	9	1	3.5	1.35	69.96	41.72	6664.1
4	16	10	1.2	4	1.46	69.73	42.65	6661.3
5	18	7	0.8	3.5	1.29	67.87	38.95	6705.1
6	18	8	0.6	4	1.37	68.84	42.31	6696.3
7	18	9	1.2	2.5	1.26	70.34	37.95	6692.8
8	18	10	1	3	1.31	70.08	39.25	6688.5
9	20	7	1	4	1.45	67.86	42.17	6761.8
10	20	8	1.2	3.5	1.39	68.98	43.21	6754.4
11	20	9	0.6	3	1.22	70.05	36.11	6751.2
12	20	10	0.8	2.5	1.1	69.57	35.56	6747.3
13	22	7	1.2	3	1.36	67.91	42.17	6811.2
14	22	8	1	2.5	1.14	69.48	35.77	6806.7
15	22	9	0.8	4	1.42	69.74	44.25	6801.9
16	22	10	0.6	3.5	1.24	68.96	36.84	6795.6

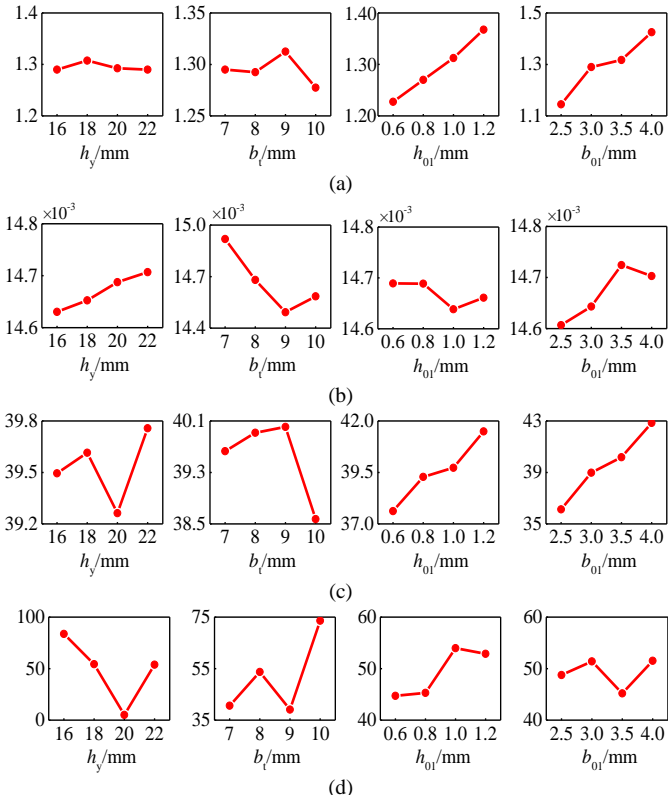


Fig. 11. Average values of (a) T_{cog} , (b) $1/T_{av}$, (c) T_{rip} , and (d) $|f_{n_6-6750}|$ under four levels of each optimization variable.

TABLE VIII
VARIANCES AND RATIOS

Parameters	Variances (ratios)			
	T_{cog}	$1/T_{av}$	T_{rip}	$ f_{n_6-6750} $
h_y	5.74E-05 (0.44%)	8.86E-04 (3.08%)	0.03 (0.41%)	796.96 (88.40%)
b_t	1.54E-04 (1.20%)	2.52E-02 (87.73%)	0.33 (4.02%)	80.05 (8.88%)
h_{01}	2.69E-03 (20.85%)	4.47E-04 (1.56%)	2.71 (33.51%)	17.89 (1.98%)
b_{01}	9.98E-03 (77.51%)	2.19E-03 (7.63%)	5.01 (62.06%)	6.61 (0.74)
Total	1.29E-02	2.87E-02	8.08	901.51

E.g,

$$y_{ov_av}(b_t = 7) = \frac{1}{4} [y_{ov}(1) + y_{ov}(5) + y_{ov}(9) + y_{ov}(13)] \quad (13)$$

The average values of T_{cog} , $1/T_{av}$, T_{rip} , and $|f_{n_6-6750}|$ under four levels of each optimization variable are shown in Fig. 11. Obviously, the level combination of each variable to make each objective optimal is different, and the variance should be analyzed to evaluate the influence of each variable on each optimization objective and their ratios, so as to obtain optimal variable combination. The variance can be calculated by [17]

$$S_{ov} = \frac{1}{4} \sum_{q=1}^4 (y_{ov_av}(q) - y_{av})^2 \quad (14)$$

where y_{av} is the total average value of a certain optimization objective. The variances of each optimization objective under different variables are arranged in Table VIII, which determine the influence levels of the change of the optimization variables on the optimization objective. Obviously, the adjustment of h_y has the greatest influence on f_{n_6} , so h_y is selected as 20mm based on the minimum $|f_{n_6-6750}|$. Similarly, b_t , h_{01} , and b_{01} can be determined based on the minimum $1/T_{av}$, T_{rip} , and T_{cog} . Finally, the optimal variable combination of $h_y=20\text{mm}$, $b_t=9\text{mm}$, $h_{01}=0.6\text{mm}$, and $b_{01}=2.5\text{mm}$ can be determined.

By narrowing the variable ranges and updating the levels of each variable according to the current optimization results, better stator parameters and corresponding performances can be obtained by designing orthogonal experiments and performing the optimization based on the Taguchi method again. Assuming that the initial range of a variable is $[a_i, b_i]$ with a step size of d_i , the optimal performance is obtained when the variable takes x_0 . The range of the variable in the next analysis can be further narrowed down to

$$\left\{ \begin{array}{l} a_{i+1} = x_0 - d_i, \quad b_{i+1} = x_0, \quad d_{i+1} = \frac{1}{3} d_i \quad \text{if } x_0 = a \\ a_{i+1} = x_0 - \frac{2}{3} d_i, \quad b_{i+1} = x_0 + \frac{1}{3} d_i, \quad d_{i+1} = \frac{1}{3} d_i \\ \quad \quad \quad \text{if } y_{om_a}(x_0 - d_i) < y_{om_a}(x_0 + d_i) \\ a_{i+1} = x_0 - \frac{3}{4} d_i, \quad b_{i+1} = x_0 + \frac{3}{4} d_i, \quad d_{i+1} = \frac{1}{2} d_i \\ \quad \quad \quad \text{if } y_{om_a}(x_0 - d_i) = y_{om_a}(x_0 + d_i) \\ a_{i+1} = x_0 - \frac{1}{3} d_i, \quad b_{i+1} = x_0 + \frac{2}{3} d_i, \quad d_{i+1} = \frac{1}{3} d_i \\ \quad \quad \quad \text{if } y_{om_a}(x_0 - d_i) > y_{om_a}(x_0 + d_i) \\ a_{i+1} = x_0, \quad b_{i+1} = x_0 + d_i, \quad d_{i+1} = \frac{1}{3} d_i \quad \text{if } x_0 = b \end{array} \right. \quad (15)$$

TABLE IX
OPTIMAL STATOR PARAMETERS AND MOTOR PERFORMANCE

	Par.	Initial	Taguchi method	Iterative Taguchi Method
Optimization variables	h_y/mm	18	20	19.55
	b_y/mm	7.7	9	8.90
	h_{01}/mm	0.8	0.6	0.65
	b_{01}/mm	3.2	2.5	2.71
Optimization objectives	$T_{\text{cog}}/(\text{N m})$	1.78	1.25	1.17
	$T_{\text{av}}/(\text{N m})$	70.86	70.24	70.47
	$T_{\text{rip}}/\%$	67.87	38.44	36.78
	$f_{n_6}/(\text{Hz})$	6699.20	6746.57	6745.31
	$a_{\max}/(\text{m/s}^2)$	2.71	1.89	1.81

TABLE X
LEVELS OF SIX VARIABLES

Variables	Level 1	Level 2	Level 3	Level 4
W_{b1}	1	1.2	1.4	1.6
W_{b2}	1	1.2	1.4	1.6
α_p	44	47	50	53
h_{sPM}	2.8	3.2	3.6	4
L_{sPM}	19.8	20.2	20.6	21
r_δ	1	2	3	4

TABLE XI
OPTIMAL ROTOR PARAMETERS AND MOTOR PERFORMANCE

	Par.	Initial	Taguchi method	Iterative Taguchi Method
Optimization variables	W_{b1}/mm	1.5	1.4	1.31
	W_{b2}/mm	1.5	1.4	1.45
	α_p/deg	48	50	50.89
	h_{sPM}/mm	3.8	3.7	3.61
Optimization objectives	L_{sPM}/mm	20.4	20.6	20.51
	r_δ	1	3	3.11
	$T_{\text{cog}}/(\text{N m})$	1.17	0.47	0.32
	$T_{\text{av}}/(\text{N m})$	70.47	68.79	68.62
	$T_{\text{rip}}/\%$	36.78	7.32	5.93
	$p_{2p86f_1}/(\text{N/m}^2)$	21.71	14.83	12.01
	$a_{\max}/(\text{m/s}^2)$	1.81	1.41	1.23

There are still 4 levels for each variable after the narrowness, new combinations can be generated according to the orthogonal table L_{16} (4^4) and analyzed by the FEM. As the step size d_{i+1} and the range $[a_{i+1}, b_{i+1}]$ are narrowed, the motor performance can be further optimized. After k iterations, when the change of the optimization objective is less than 1% between two adjacent optimizations, the iteration of the optimization variable that has the greatest impact on it is ended and the optimal results are outputted.

For example, assume that the optimal ranges for 4 variables are all [1, 7], and the optimal values are all 3. According to the orthogonal table L_{49} (7^4), the conventional Taguchi method needs to be calculated 49 combinations to obtain the optimal values for the optimization of 4 variables and 7 levels. The improved iterative Taguchi method proposed in this paper only needs to iterate once for the optimization of 4 variables and 3 levels according to the orthogonal table L_9 (3^4), and the optimal values can be obtained by calculating 9 combinations for the first time and 16 combinations for the second time, and the efficiency is increased by 96%. It is worth noting that when a variable first reaches the optimum, the optimization variables in the subsequent optimization process are reduced, and the efficiency of the orthogonal experiment is further improved.

The optimal stator parameters determined by the improved iterative Taguchi method are given in Table IX. Compared with the conventional Taguchi method, the optimization efficiency and effect are greatly improved. Based on the optimal stator parameters, the skewed stator core with the stator teeth inclined by one pitch is further designed to improve the electromagnetic performances of the motor, which basically does not change the natural frequencies of the stator. Avoid directly modeling and optimizing the three-dimensional skewed stator, the optimization efficiency is greatly improved, and the change ranges of motor performances are clearer. If the optimization objective $|f_{n_6}-6750|$ is changed to p_{2p86f_1} in the objective function \min_1 during the optimization stage of stator parameters, the overall optimization effect will deteriorate and the maximum vibration acceleration will increase by 24.86%.

2) Rotor parameter optimization

Six independent rotor parameters are selected as optimization variables in the second optimization stage, and the levels of each variable are shown in Table X. The orthogonal experiments of 6 variables and 4 levels are designed based on the orthogonal table L_{32} (4^6), and the corresponding performances of 32 variable combinations are analyzed by the FEM. The optimization results of the rotor parameters based on the improved iterative Taguchi method are shown in Table XI. Finally, the optimal structural parameters of the 6-pole 36-slot IPMSM with a non-uniform air gap are quickly determined.

V. OPTIMIZATION RESULTS AND EXPERIMENTAL VERIFICATION

A. Comparison of optimization results

In order to avoid the reduction of the fundamental amplitude of no-load back EMF caused by the increase of air gap after the rotor optimization, the lengths of PMs in the optimized IPMSM are increased to 19.6mm. The no-load back EMFs and their harmonic contents of the IPMSMs with skewed stators before and after optimization are compared in Fig. 12. It can be seen that all harmonics except the 3rd harmonic in the no-load back EMF optimized by the iterative Taguchi method are eliminated.

The cogging torques, output torques, and electromagnetic vibrations of the IPMSMs with skewed stators before and after optimization are respectively shown in Fig. 13(a), Fig. 13(b), and Fig. 14. The cogging torque is reduced by 74.6% from 0.63 N m to 0.16 N m, and the torque ripple is also effectively reduced. In addition, the electromagnetic vibrations of the motor are greatly improved, and the maximum vibration accelerations with no load and rated load are reduced by 46.82% and 41.96% respectively. What's more, compared with the conventional Taguchi method, the improved iterative Taguchi method can obtain the optimal structural parameters of the motor on the basis of ensuring the optimization efficiency, the cogging torque and torque ripple are smaller, the average output torque is greater and the no-load back EMF is more ideal, the overall performance is greatly improved.

Further, the losses and temperature distribution of each part of the optimal motor are explored in Fig. 15 and Fig. 16, respectively. The copper loss of the motor can be directly calculated from the rated current and phase resistance, which is 383.2W. Due to the relatively low overall temperature distribution of the motor, the conventional heat dissipation

method of air cooling is adopted. The temperature of windings is the highest due to the relatively high copper loss, the temperature of the PMs does not exceed 50°C, and the temperature of all parts of the motor is in a safe area. In addition, the power factor of the optimal motor is 0.963, and the efficiency reaches 0.935. To ensure the safe and reliable operation of the motor, the irreversible demagnetization of PMs under different working conditions is evaluated. The demagnetization ratio coefficients of PMs under different working conditions are shown in Table XII. The demagnetization ratio coefficient is defined as the reduction degree of the no-load back EMF after demagnetization, which is

$$K = \frac{E_1 - E_{1d}}{E_1} \times 100\% \quad (16)$$

where E_1 and E_{1d} are the effective values of the no-load back EMFs before and after demagnetization. To investigate the demagnetization law of the PMs under extremely harsh working conditions, the demagnetization currents are applied in the d-axis direction. It can be seen from Table XII that even if the demagnetization current is 5 times the rated current, the PMs will not undergo irreversible demagnetization at 20°C. When the temperatures of the PMs are 150°C and the d-axis demagnetization current is the rated current, the irreversible demagnetization occurs at the corners of the PMs, but the overall demagnetization ratio is low, which has little impact on the motor performance. Continuing to increase the d-axis demagnetization current to 4 times the rated current, the demagnetization ratio coefficient of the PMs reaches 99.32% at 150°C, and almost all PMs are demagnetized. Therefore, it is necessary to strictly avoid the PMs working under ultra-high temperature and ultra-high current, but the irreversible demagnetization degree of the PMs is very slight only under short-term low temperature and high current or high temperature and rated current, and the change of the overall performance of the motor is also small.

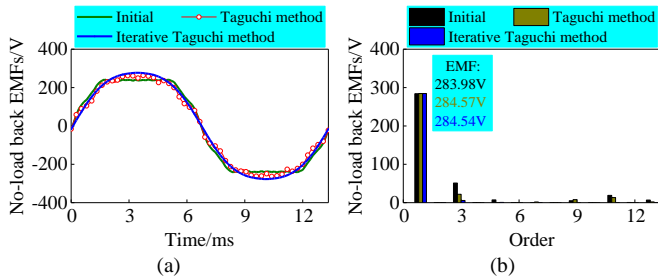


Fig. 12. Comparisons of (a) no-load back EMFs and (b) their harmonic contents before and after optimization.

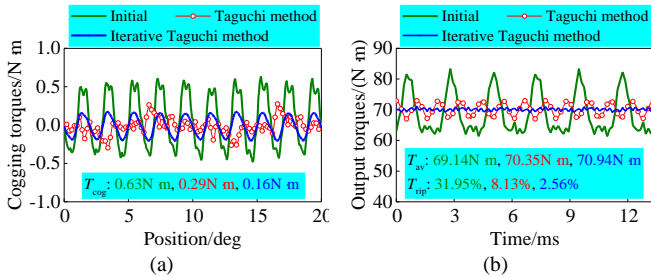


Fig. 13. Comparisons of (a) cogging torques and (b) output torques before and after optimization.

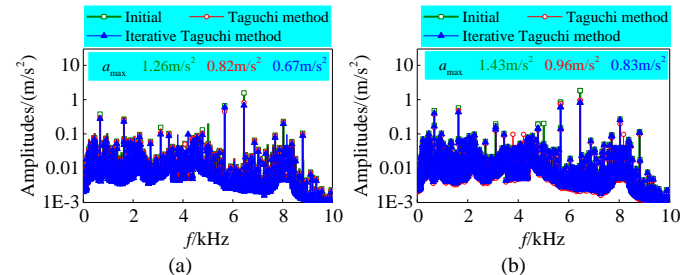


Fig. 14. Comparisons of vibration accelerations of the motor with (a) no load and (b) rated load.

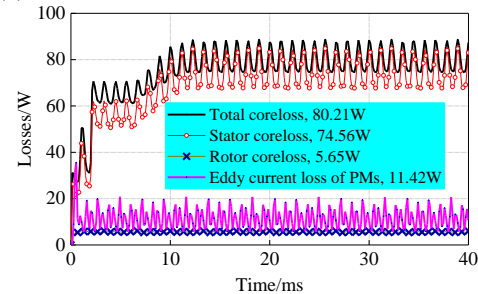


Fig. 15. Losses of each part of the optimal motor.

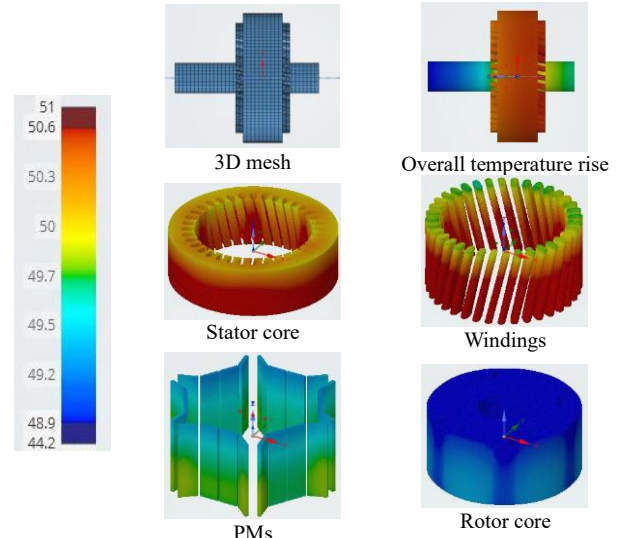


Fig. 16. Temperature distribution of each part of the optimal motor.

TABLE XII
DEMAGNETIZATION RATIO COEFFICIENT UNDER DIFFERENT WORKING CONDITIONS

Working conditions	Irreversible demagnetization regions	Demagnetization ratio coefficients
Rated current and 20°C		0
5 times the rated current and 20°C		0
Rated current and 150°C		7.89%
2 times the rated current and 150°C		68.56%
4 times the rated current and 150°C		99.32%

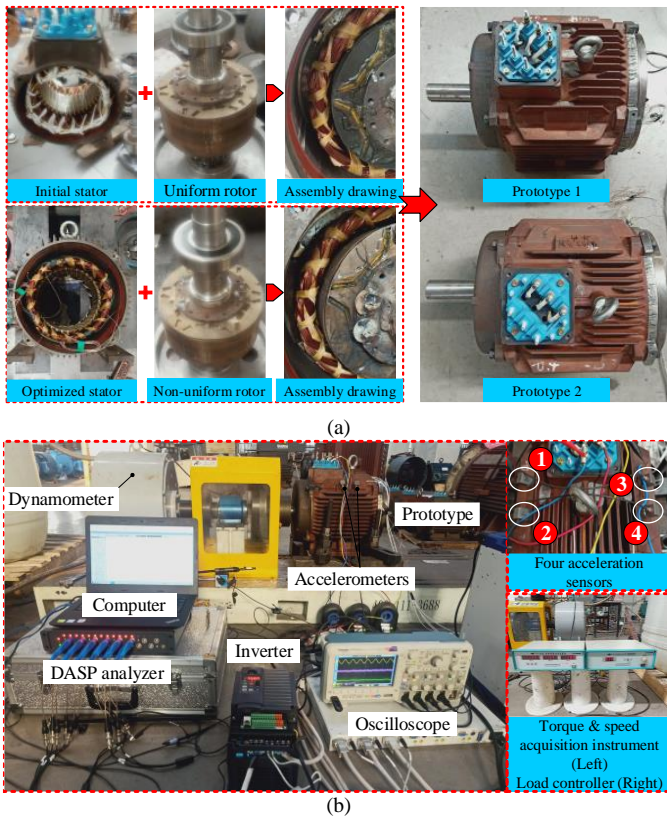


Fig. 17. Performance test. (a) Two prototypes. (b) Test platform.

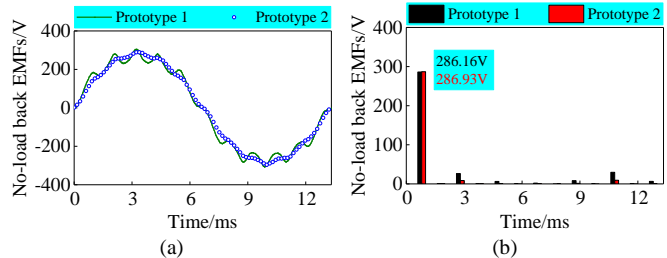


Fig. 18. Comparisons of (a) no-load back EMFs and (b) their harmonic contents of two prototypes.

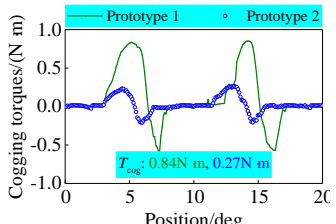


Fig. 19. Comparisons of cogging torques of two prototypes.

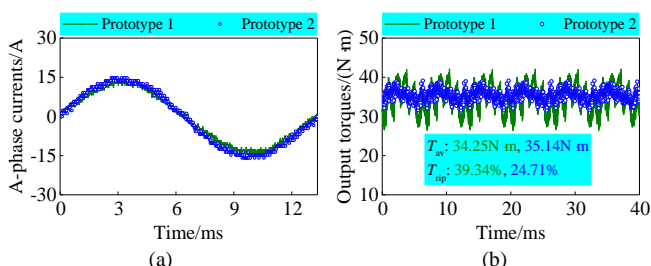


Fig. 20. Comparisons of (a) A-phase currents and (b) output torques of two prototypes at 1500r/min with 0.5 times rated load corresponding to 1500r/min.

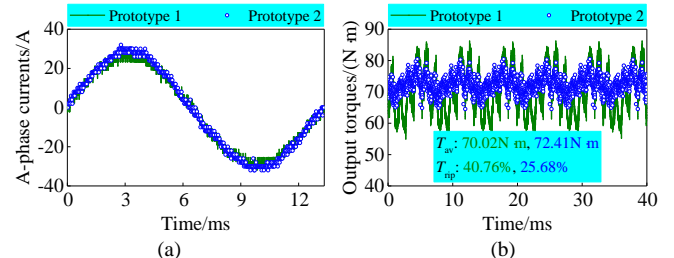


Fig. 21. Comparisons of (a) A-phase currents and (b) output torques of two prototypes at 1500r/min with the rated load corresponding to 1500r/min.

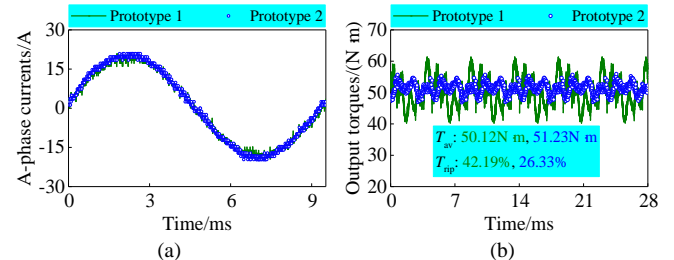


Fig. 22. Comparisons of (a) A-phase currents and (b) output torques of two prototypes at 2100r/min with the rated load corresponding to 2100r/min.

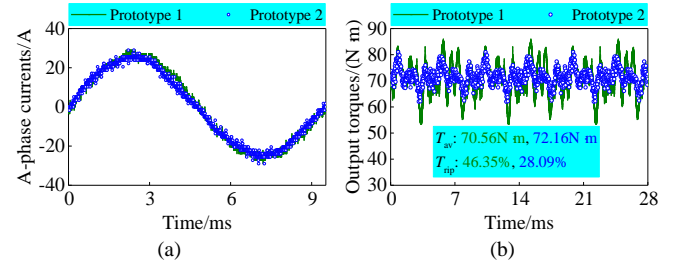


Fig. 23. Comparisons of (a) A-phase currents and (b) output torques of two prototypes at 2100r/min with the rated load corresponding to 1500r/min.

B. Electromagnetic performance test

Two prototypes with skewed stators before and after optimization are produced to clearly compare the optimization effect of structural parameters of stator and rotor except for the influence of skewed slots, and sufficient experiments are performed. The stator and rotor of the prototypes are shown in Fig. 17(a), and the performance test platform of the prototypes is shown in Fig. 17(b). The test results of A-phase no-load back EMFs of two prototypes at 1500r/min are compared in Fig. 18. Consistent with the analytical results, the amplitude of each harmonic component of the no-load back EMF of the optimized motor is lower. Connect the torque sensor to the prototype, and the torque output analog signal of the torque sensor is directly collected by the DASP analyzer with a high sampling frequency. The cogging torque test results of the two prototypes are shown in Fig. 19. Due to the installation error of the torque sensor and its own accuracy, and the difficulty of manually rotating the mechanical shaft to achieve complete uniform speed, the maximum positive values of the test results are greater than the minimum negative values (comparison of absolute values). Although there is some error in the results measured based on the simple testing platform, the test result of prototype 2 is significantly smaller than that of prototype 1, which effectively proves the effectiveness of the optimal parameters in reducing the cogging torque. The A-phase

currents and output torques of two prototypes at 1500r/min and 2100r/min are shown in Fig. 20 to Fig. 23. Whether the prototypes operate at a rated speed of 1500r/min or a higher speed of 2100r/min, the torque ripples of the optimized prototype are smaller. The high-frequency harmonics of the test currents are relatively rich due to the influence of the modulation mode of the inverter. The no-load back EMFs, cogging torques, average torques, and torque ripples obtained by the FEM and prototype testing are compared in Table XIII. The amplitudes of the fundamental components of the no-load back EMFs and average torques obtained by the two methods are basically consistent. The test results of the cogging torques are slightly larger than the finite element results. Due to small assembly errors such as rotor misalignment and eccentricity and the influence of rotor torsional vibrations, the tested torque ripples are significantly greater than that obtained by the FEM. However, the cogging torque and torque ripple of the optimized motor are greatly reduced on the basis of heightening the output torque.

C. Vibration test

The modal test platform of the stator cores is established based on the hammering method, as shown in Fig. 24. The calculated and measured natural frequencies of the straight and skewed stator cores are shown in Table XIV, respectively.

TABLE XIII
COMPARISON OF MOTOR PERFORMANCE

	Prototype 1		Prototype 2	
	FEM	Prototype testing	FEM	Prototype testing
Fundamental components of no-load back EMFs/V (Error)	283.98 (0.76%)	286.16	284.54 (0.83%)	286.93
Average torques/N m (Error)	69.14 (1.26%)	70.02	70.94 (2.03%)	72.41
Cogging torques/N m	0.63	0.84	0.16	0.27
Torque ripples/%	31.95	40.76	2.56	25.68

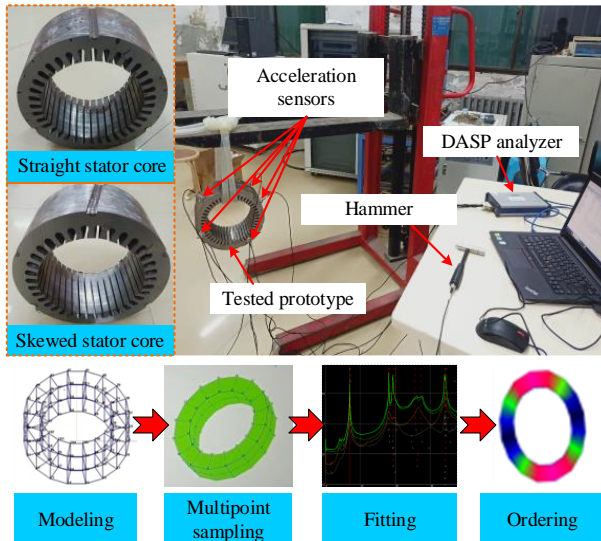


Fig. 24. Modal test platform of the stator core.

TABLE XIV

NATURAL FREQUENCIES OF STRAIGHT AND SKEWED STATOR CORES

Order	Modal shapes	Straight stator core	Skewed stator core
2nd		FEM 677.01Hz	FEM 677.86Hz
		Test 690.20Hz	Test 691.82Hz
		Error -1.91%	Error -2.06%
3rd		FEM 1776.80Hz	FEM 1778.65Hz
		Test 1799.91Hz	Test 1803.73Hz
		Error -1.28%	Error -1.41%
4th		FEM 3347.40Hz	FEM 3356.30Hz
		Test 3452.53Hz	Test 3455.98Hz
		Error -3.04%	Error -2.97%

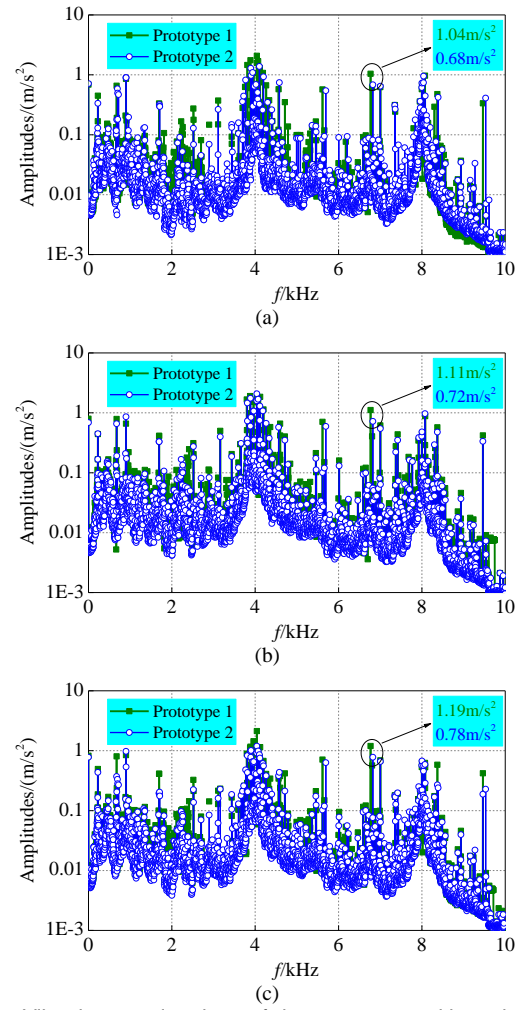


Fig. 25. Vibration accelerations of the prototypes with no load at (a) 750r/min, (b) 1500r/min, and (c) 2100r/min.

TABLE XV
COMPARISON OF VIBRATION ACCELERATIONS

	Prototype 1		Prototype 2	
	FEM	Prototype testing	FEM	Prototype testing
750r/min /(m/s ²) (Error)	1.15 (10.57%)	1.04	0.62 (8.82%)	0.68
1500r/min /(m/s ²) (Error)	1.26 (13.51%)	1.11	0.67 (6.94%)	0.72
2100r/min /(m/s ²) (Error)	1.35 (13.44%)	1.19	0.76 (2.56%)	0.78

Compared with the test results, the errors of the natural frequencies obtained by the FEM are not more than 3.1%, which have high accuracy. In addition, the natural frequencies of the straight and skewed stator cores are close, thus replacing the skewed stator with the straight stator in the process of stator parameter optimization can improve the optimization efficiency without affecting the optimization effect.

The measured vibration accelerations of the prototypes with no load at 750r/min, 1500r/min, and 2100r/min are compared in Fig. 25. There are rich acceleration responses around the switching frequency (which is 4kHz in this paper), but they can be effectively reduced by increasing the switching frequency or adopting random switching frequency, which is not considered temporarily in the motor optimization design stage. The vibration accelerations obtained by the FEM and prototype testing are compared in Table XV. Due to the influence of the end covers and the errors in stator structure and material parameters, the natural frequencies of the prototype deviate slightly from the results obtained by the FEM, and the extreme values of the vibration acceleration also deviate slightly. However, the vibration accelerations near the 6th-order natural frequency of the stator are effectively reduced at different speeds, which well verifies the proposed optimization method and optimized motor parameters.

VI. CONCLUSION

In this paper, a 6-pole 36-slot IPMSM with a non-uniform air gap is designed and then comprehensively optimized for the low-level torque ripple and electromagnetic vibration. During the motor optimization process, the optimization variables of the stator and rotor are stratified, and the optimization objectives in each level are selected according to relevance and sensitivity, which greatly improves the optimization efficiency and effect. In addition, an improved iterative Taguchi method is proposed. Compared with the conventional Taguchi method, the method proposed in this paper can achieve better optimization results on the basis of greatly improving the optimization efficiency, and the overall performance and reliability of IPMSM are greatly improved, the temperature distribution of each part of the motor and the risk of irreversible demagnetization of the PMs at the extreme temperature are within the safe range. Finally, the test platform of the prototype is established, and sufficient experiments are carried out, the validity and accuracy of the optimization results are well verified by the prototype tests.

Reference

- [1] V. Ruuskanen, J. Nerg, M. Rilla and J. Pyrhönen, "Iron Loss Analysis of the Permanent-Magnet Synchronous Machine Based on Finite-Element Analysis Over the Electrical Vehicle Drive Cycle," *IEEE Trans. Ind. Electron.*, vol. 63, no. 7, pp. 4129-4136, July 2016.
- [2] D. Wang, C. Peng, J. Li and C. Wang, "Comparison and Experimental Verification of Different Approaches to Suppress Torque Ripple and Vibrations of Interior Permanent Magnet Synchronous Motor for EV," *IEEE Trans. Ind. Electron.*, 2022.
- [3] S. Wu, D. D. Reigosa, Y. Shibukawa, M. A. Leetmaa, R. D. Lorenz and Y. Li, "Interior Permanent-Magnet Synchronous Motor Design for Improving Self-Sensing Performance at Very Low Speed," *IEEE Trans. Ind. Appl.*, vol. 45, no. 6, pp. 1939-1946, Nov. 2009.
- [4] K. Kim, "A Novel Method for Minimization of Cogging Torque and Torque Ripple for Interior Permanent Magnet Synchronous Motor," *IEEE Trans. Mag.*, vol. 50, no. 2, pp. 793-796, Feb. 2014.
- [5] K. C. Kim, D. H. Koo, J. P. Hong and J. Lee, "A Study on The Characteristics Due to Pole-Arc to Pole Pitch Ratio and Saliency to Improve Torque Performance of IPMSM," *IEEE Trans. Magn.*, vol. 43, no. 6, pp. 2516-2518, Jun. 2007.
- [6] D. Barman and P. Pillay, "Effect of Skewing in a Variable Flux Interior Permanent Magnet Synchronous Machine," *IEEE Trans. on Ind. Appl.*, vol. 56, no. 6, pp. 6399-6410, Nov.-Dec. 2020.
- [7] C. Peng, D. Wang, Z. Feng and B. Wang, "A New Segmented Rotor to Mitigate Torque Ripple and Electromagnetic Vibration of Interior Permanent Magnet Machine," *IEEE Trans. Ind. Electron.*, vol. 69, no. 2, pp. 1367-1377, Feb. 2022.
- [8] X. Sun, Z. Shi, G. Lei, Y. Guo and J. Zhu, "Multi-Objective Design Optimization of an IPMSM Based on Multilevel Strategy," *IEEE Trans. Ind. Electron.*, vol. 68, no. 1, pp. 139-148, Jan. 2021.
- [9] P. Akiki *et al.*, "Multiphysics Design of a V-Shape IPM Motor," *IEEE Trans. Energy Convers.*, vol. 33, no. 3, pp. 1141-1153, Sept. 2018.
- [10] G. Lei, C. Liu, J. Zhu, and Y. Guo, "Techniques for Multilevel Design Optimization of Permanent Magnet Motors," *IEEE Trans. Energy Convers.*, vol. 30, no. 4, pp. 1574-1584, Dec. 2015.
- [11] C. Ma, *et al.*, "Sound Quality Evaluation of Noise of Hub Permanent-Magnet Synchronous Motors for Electric Vehicles," *IEEE Trans. Ind. Electron.*, vol. 63, no. 9, pp. 5663-5673, 2016.
- [12] C. Ma, Q. Li, L. Deng, C. Chen, Q. Liu and H. Gao, "A Novel Sound Quality Evaluation Method of the Diagnosis of Abnormal Noise in Interior Permanent-Magnet Synchronous Motors for Electric Vehicles," *IEEE Trans. Ind. Electron.*, vol. 64, no. 5, pp. 3883-3891, 2017.
- [13] F. Liu, X. Wang, Z. Xing, J. Ren and X. Li, "Analysis and Research on No-Load Air Gap Magnetic Field and System Multiobjective Optimization of Interior PM Motor," *IEEE Trans. Ind. Electron.*, vol. 69, no. 11, pp. 10915-10925, Nov. 2022.
- [14] B. Yan, Y. Yang and X. Wang, "Design of a Large Capacity Line-Start Permanent Magnet Synchronous Motor Equipped With Hybrid Salient Rotor," *IEEE Trans. Ind. Electron.*, vol. 68, no. 8, pp. 6662-6671, 2021.
- [15] X. Zhu, W. Wu, L. Quan, Z. Xiang and W. Gu, "Design and Multi-Objective Stratified Optimization of a Less-Rare-Earth Hybrid Permanent Magnets Motor With High Torque Density and Low Cost," *IEEE Trans. Energy Convers.*, vol. 34, no. 3, pp. 1178-1189, Sept. 2019.
- [16] S. S. R. Bonthu, S. Choi and J. Baek, "Design Optimization With Multiphysics Analysis on External Rotor Permanent Magnet-Assisted Synchronous Reluctance Motors," *IEEE Trans. Energy Convers.*, vol. 33, no. 1, pp. 290-298, March 2018.
- [17] X. Sun, Z. Shi and J. Zhu, "Multiobjective Design Optimization of an IPMSM for EVs Based on Fuzzy Method and Sequential Taguchi Method," *IEEE Trans. Ind. Electron.*, vol. 68, no. 11, pp. 10592-10600, Nov. 2021.
- [18] B. Zhang, A. Wang and M. Doppelbauer, "Multi-Objective Optimization of a Transverse Flux Machine With Claw-Pole and Flux-Concentrating Structure," *IEEE Trans. Mag.*, vol. 52, no. 8, pp. 1-10, Aug. 2016.
- [19] S. Wu, S. Zuo and Y. Zhang, "Optimization for Electromagnetic Noise Reduction in Claw Pole Alternator by Rotor Claw Chamfering," *IEEE Trans. Ind. Electron.*, vol. 65, no. 12, pp. 9325-9335, Dec. 2018.
- [20] Z. Xing, X. Wang and W. Zhao, "Optimization of Stator Slot Parameters for Electromagnetic Vibration Reduction of Permanent Magnet Synchronous Motors," *IEEE Trans. Transpor. Electri.*, vol. 8, no. 4, pp. 4337-4347, Dec. 2022.
- [21] Z. Xing, X. Wang, and W. Zhao, "An Accurate Calculation Method of Natural Frequencies of the Radial-Flux Slotted Motors Considering End Covers," *IEEE Trans. Ind. Electron.*, vol. 70, no. 6, pp. 5516-5526, June 2023.
- [22] C. Ma *et al.*, "Analytical Model of Open-Circuit Air-Gap Field Distribution in Interior Permanent Magnet Machines Based on Magnetic Equivalent Circuit Method and Boundary Conditions of Macroscopic Equations," *IEEE Trans. Mag.*, vol. 57, no. 3, pp. 1-9, March 2021.
- [23] H. Kim, A. Posa, J. Nerg, J. Heikkilä and J. T. Sopanen, "Analysis of Electromagnetic Excitations in an Integrated Centrifugal Pump and Permanent Magnet Synchronous Motor," *IEEE Trans. Energy Conv.*, vol. 34, no. 4, pp. 1759-1768, Dec. 2019.
- [24] F. Lin, S. Zuo, W. Deng, and S. Wu, "Modeling and Analysis of Electromagnetic Force, Vibration and Noise in Permanent-Magnet Synchronous Motor Considering Current Harmonics," *IEEE Trans. Ind. Electron.*, vol. 63, no. 12, pp. 7455-7466, 2016.

- [25] X. Liu, H. Chen, J. Zhao, and A. Belahcen, "Research on The Performances and Parameters of Interior PMSM Used for Electric Vehicles," *IEEE Trans. Ind. Electron.*, vol. 63, no. 6, pp. 3533-3545, 2016.
- [26] D. K. Lim, and J. S. Ro, "Analysis and Design of a Delta-Type Interior Permanent Magnet Synchronous Generator by Using an Analytic Method," *IEEE Access*, vol. 7, pp. 85139-85145, 2019.
- [27] Q. Ma, A. El-Refaie and B. Lequesne, "Low-Cost Interior Permanent Magnet Machine With Multiple Magnet Types," *IEEE Trans. on Ind. Appl.*, vol. 56, no. 2, pp. 1452-1463, 2020.
- [28] Z. Xing, X. Wang, and W. Zhao, "Cogging Torque Reduction Based on Segmented Skewing Magnetic Poles with Different Combinations of Pole-Arc Coefficients in Surface-Mounted Permanent Magnet Synchronous Motors," *IET Elect. Power Appl.*, vol. 15, no. 2, pp. 200-213, 2021.
- [29] Y. Lu, J. Li, and K. Yang, "A hybrid calculation method of electromagnetic vibration for electrical machines considering high-frequency current harmonics," *IEEE Trans. Ind. Electron.*, vol. 69, no. 10, pp. 10385-10395, 2022.